Particle size distribution and morphological changes in activated carbon-metal oxide hybrid catalysts prepared under different heating conditions

A. BARROSO-BOGEAT, M. ALEXANDRE-FRANCO, C. FERNÁNDEZ-GONZÁLEZ & V. GÓMEZ-SERRANO

Department of Organic and Inorganic Chemistry, Faculty of Sciences, University of Extremadura, Badajoz, Spain

Summary

In catalysis processes, activated carbon (AC) and metal oxides (MOs) are widely used either as catalysts or as catalyst supports because of their unique properties. A combination of AC and a MO in a single hybrid material entails changes not only in the composition, microstructure and texture but also in the morphology, which may largely influence the catalytic behaviour of the resulting product. This work is aimed at investigating the modifications in the morphology and particle size distribution (PSD) for AC-MO hybrid catalysts as a result of their preparation under markedly different heating conditions. From a commercial AC and six MO (Al_2O_3, Fe_2O_3, ZnO, SnO_2, TiO_2 and WO_3) precursors, two series of such catalysts are prepared by wet impregnation, oven-drying at 120ºC, and subsequent heat treatment at 200ºC or 850ºC in inert atmosphere. The resulting samples are characterized in terms of their morphology and PSD by scanning electron microscopy and ImageJ processing program. Obtained results indicate that the morphology, PSD and degree of dispersion of the supported catalysts are strongly dependent both on the MO precursor and the heat treatment temperature. With the temperature rise, trends are towards the improvement of crystallinity, the broadening of the PSD and the increase in the average particle size, thus suggesting the involvement of sintering mechanisms. Such effects are more pronounced for the Fe, Sn and W catalysts due to the reduction of the corresponding MOs by AC during the heat treatment at 850ºC.

Introduction

Activated carbon (AC) has been widely used as catalyst on its own right and more commonly as catalyst support due to a number of unique and excellent properties, which have been extensively reviewed and discussed elsewhere (Rodríguez-Reinoso, 1998; Serp & Figueiredo, 2009). Metal oxides (MOs) are one of the most important and employed categories of solid catalysts, being also used either as active phases or as supports because of their acid base and redox properties, low-cost production, easy regeneration and selective action (Henrich & Cox, 1994). Therefore, it becomes apparent that the combination of AC and MOs in a single hybrid material may lead to significant and advantageous changes in the catalytic behaviour and performance, which would redound to the number of applications. Thus, AC-supported MO hybrid materials are widely used as heterogeneous catalysts for a number of industrially relevant chemical reactions, which have been recently reviewed elsewhere (Barroso-Bogeat *et al.*, 2011).

It is generally agreed that the catalytic activity of the aforesaid AC-MO hybrid catalysts is the result of a complex interplay between several factors, including not only the specific activities and relative contents of AC and MOs in the samples, but also other factors concerning their texture and morphology. Among the latter, the shape, size distribution, crystalline or amorphous nature and dispersion of the MO particles on the AC surface have been recognized to play a key role. A high degree of dispersion of the active phase is essential as it usually enhances the catalytic efficiency (Rodríguez-Reinoso, 1998). In this connection, AC is widely used as catalyst support because its large surface area and well-developed porosity allow preparing supported catalysts with a great dispersion of the active phase, which prevents it from sintering when operating at high temperatures (Rodríguez-Reinoso, 1998).

The catalytic activity of the supported MOs is also strongly influenced by their particle size, which depends on the crystal nucleation and growth processes, giving rise to different particle size distributions (PSDs). Furthermore, it has been reported that heterogeneous catalysts usually undergo a growth in particle size when operating in reaction environments at

Correspondence to: A. Barroso-Bogeat, Department of Organic and Inorganic Chemistry, University of Extremadura, Avda. de Elvas s/n, E-06006 Badajoz, Spain. Tel: +34-924-289421; fax: +34-924-271449; e-mail: adrianbogeat@unex.es

high temperatures, so that the PSDs show a long tail to the right, i.e. particles having sizes markedly larger than the mean (Benavidez *et al.*, 2012). The origin of this particle growth is still unclear and two limiting mechanisms have been proposed to explain it: particle migration and Ostwald ripening (Datye *et al.*, 2006). As a rule, the formation of large particles of the active phase in industrial-supported catalysts is undesirable because of their low reactivity, which redounds in detrimental economic consequences (Benavidez *et al.*, 2012). Another important factor when preparing AC-supported MO catalysts is the uniformity of the dispersion of the catalyst precursor, since it has been suggested that the formation of large MO particles is likely to arise from nonuniform distributions of the catalyst precursor. Therefore, it is evident that the control of the PSD for AC-supported MOs during not only the preparation but also the operation is a pivotal factor in order to achieve high and long-term catalytic performances.

This work is aimed at investigating the changes occurring in the morphology and PSD of a broadly varied series of AC-MO hybrid catalysts as a result of their preparation under markedly different heating conditions. Since catalysis processes usually require to heat at relatively high temperatures (Rodríguez-Reinoso, 1998), at which physicochemical properties of the catalysts may undergo relevant modifications and thereby influence their catalytic behaviour, two series of hybrid catalysts were prepared by heating at very different temperatures (i.e. 200ºC and 850ºC). The resulting samples are characterized in terms of their morphology by scanning electron microscopy (SEM). Obtained micrographs are processed and analyzed with aid of ImageJ free software in order to estimate the PSD for each of the prepared catalysts. The results in this paper complement those of the textural and microstructural characterization previously carried out for these hybrid catalysts and recently reported elsewhere (Barroso-Bogeat *et al.*, 2014, 2015).

Materials and methods

Materials and reagents

A granular AC purchased from Merck®(Darmstadt, Germany), 1.5 mm average particle size (Cod. 1.02514.1000), as received without any further treatment, was used as support of a broadly varied series of MOs, including Al_2O_3, Fe_2O_3, ZnO, SnO_2, TiO_2 and WO_3. The selected MO precursors were $Al(NO_3)_3 \cdot 9H_2O$, $Fe(NO_3)_3 \cdot 9H_2O$, $Zn(NO_3)_2 \cdot 6H_2O$, $SnCl_2 \cdot 2H_2O$ and $Na_2WO_4 \cdot 2H_2O$, all of them supplied by Panreac® (Barcelona, Spain) and being of reagent grade. As an exception to the rule, anatase powder from Aldrich® (Steinheim, Germany), less than 325 mesh average particle size, was employed as TiO_2 precursor.

Preparation of AC-MO hybrid catalysts

The preparation of the AC-MO hybrid catalysts was performed following the procedures previously described in detail else-

Table 1. Methods of preparation and sample codes for AC-MO hybrid catalysts

Series	Precursor	MHTT/ºC	t/h	A	Code
Series 1	$Al(NO_3)_3 \cdot 9H_2O$	200	2	N_2	A200
	$Fe(NO_3)_3 \cdot 9H_2O$	200	2	N_2	F200
	$Zn(NO_3)_2 \cdot 6H_2O$	200	2	N_2	Z200
	$SnCl_2 \cdot 2H_2O$	200	2	N_2	S200
	TiO_2 anatase	200	2	N_2	T200
	$Na_2WO_4 \cdot 2H_2O$	200	2	N_2	W200
Series 2	$Al(NO_3)_3 \cdot 9H_2O$	850	2	N_2	A850
	$Fe(NO_3)_3 \cdot 9H_2O$	850	2	N_2	F850
	$Zn(NO_3)_2 \cdot 6H_2O$	850	2	N_2	Z850
	$SnCl_2 \cdot 2H_2O$	850	2	N_2	S850
	TiO_2 anatase	850	2	N_2	T850
	$Na_2WO_4 \cdot 2H_2O$	850	2	N_2	W850

Abbreviations: MHTT, maximum heat treatment temperature; t, isothermal time at MHTT; A, atmosphere.

where (Barroso-Bogeat *et al.*, 2014, 2015), which are briefly summarized in Table 1 together with the codes assigned to the resulting products. Accordingly, as a whole, two series of hybrid catalysts were prepared (i.e. two of these samples with each MO precursor) depending on heating conditions. They are named as series 1 (200ºC, 2 h) and series 2 (850ºC, 2 h). In addition, for comparison purposes, two samples were obtained by heating only AC, in the absence of any MO precursor, under identical conditions as in the preparation of the hybrid catalysts. Such samples are henceforth referred to as AC200 and AC850 in the text.

Characterization of AC-MO hybrid catalysts

Ash content. The ash content of AC and the prepared AC-MO hybrid catalysts was determined by incineration at 650ºC for about 12 h in air, using a muffle furnace (Selecta®, Barcelona, Spain). The results have been reported elsewhere (Barroso-Bogeat *et al.*, 2015) and are compiled in Table 2.

X-ray diffraction (XRD). The crystalline metal phases present in each hybrid catalyst were investigated by powder XRD, using a D8 Bruker Advance® diffractometer working with Cu Kα radiation ($\lambda = 1.5406$ Å). The patterns were registered in the step scanning mode of 0.02º (2θ) and 0.5 s step^{-1} counting time, within the range from 10º to 80º. The identification of the crystalline phases was accomplished by comparing peak positions and intensities with standard JCPDS files and with data previously reported in literature. The average crystallite size (D) was estimated for each of the crystalline phases in the samples by applying the Scherrer equation (Cullity, 1959) to their characteristic diffraction peaks

$$D = \frac{K \cdot \lambda}{\beta \cdot cos\theta} \tag{1}$$

Table 2. Ash content, crystalline phases and their mean crystallite size (D) for the prepared AC-MO hybrid catalysts

Sample	Ash content/wt.%	Crystalline phase	D/nm	Sample	Ash content/wt.%	Crystalline phase	D/nm
A200	8.86	Alumina (Al_2O_3)	1.88	A850	5.68	Corundum (α-Al_2O_3)	2.06
F200	13.55	Hematite (α-Fe_2O_3)	3.22			Hematite (α-Fe_2O_3)	36.60
		Goethite (α-$FeO(OH)$)	3.17	F850	14.66	Magnetite (γ-Fe_2O_3)	15.11
		Maghemite (Fe_3O_4)	6.19			Iron (Fe)	
S200	27.21	Cassiterite (SnO_2)	4.05	S850	2.34	Cassiterite (SnO_2)	36.16
		Romarchite (SnO)	5.07			Tin (Sn)	89.62
T200	8.05	Anatase (TiO_2)	3.53			Anatase (TiO_2)	2.31
W200	9.93	Tungsten oxide (WO_3)	2.37	T850	9.33	Rutile (TiO_2)	1.86
		Tungstite ($WO_3 \cdot H_2O$)	3.05	W850	11.54	Tungsten (W)	48.36
Z200	9.45	Zincite (ZnO)	20.80			Tungsten carbide ($W_6C_{2.54}$)	3.67
		Wülfingite (ε-$Zn(OH)_2$)	1.89	Z850	6.18	Zincite (ZnO)	69.38

where K is the Scherrer constant ($K = 0.94$), λ is the wavelength of the X-ray radiation, β denotes the full-width at half-maximum of the diffraction peak and θ is the characteristic Bragg angle of the crystalline phase.

The powder XRD patterns for the prepared hybrid catalysts, together with the main crystalline phases and their average crystallite size, have been recently reported elsewhere (Barroso-Bogeat *et al.*, 2015), and the results are also collected in Table 2. Regarding this, it should be noted that the Scherrer equation is limited to particles having sizes in the nanoscale, so that it is not applicable to grains larger than about 0.1 to 0.2 μm. Furthermore, the Scherrer equation only provides a lower bound for the crystallite size. This fact is likely related with a number of factors contributing to the width of the diffraction peaks besides the instrumental effects and the crystallite size. Among them, the most important ones are usually inhomogeneous strain and crystal lattice imperfections. Other sources of peak broadening are dislocations, stacking faults, twinning, microstresses, grain boundaries, chemical heterogeneities and so on (Singh, 2005). Because of these contributions to the peak width are nonzero, it becomes apparent that the crystallite size will be larger than that estimated by the Scherrer equation.

Textural

The textural characterization of AC, AC heat-treated samples and the prepared AC-MO hybrid catalysts was carried out by N_2 adsorption at -196ºC and mercury porosimetry. The specific surface area (S_{BET}) and micropore volume (W_0) were estimated by applying the Brunauer, Emmet and Teller (BET) equation (Brunauer *et al.*, 1938) and the Dubinin-Radushkevich equation (Dubinin, 1975), respectively, to the experimental N_2 isotherms measured in a semiautomatic adsorption equipment (Autosorb 1, Quantachrome®). The mesopore (V_{me}) and macropore (V_{ma}) volumes were derived from the mercury intrusion curves obtained in a mercury porosimeter (PoreMaster-60, Quantachrome®). Finally, the total pore volume (V_T') was calculated from W_0, V_{me} and V_{ma}. These textural data have been recently reported in a previous work (Barroso-Bogeat *et al.*, 2014) and are set out in Table 3.

Morphological

Electron microscope images were obtained with a scanning electron microscope model Quanta 3D FEG (FEI Company®) operating in the high vacuum mode under an accelerating voltage ranging from 0.2 to 30 kV, and using an Everhart-Thornley detector for secondary electrons. The sample, as prepared without any further treatment, was mounted onto an aluminium specimen stub with aid of a conductive carbon adhesive. The SEM microscope was also attached with an energy dispersive X-ray (EDX) analysis detector to determine the surface elemental composition of the hybrid catalysts under study.

In this work, a set of 4 to 8 SEM images in random regions were acquired for each sample at different magnification levels, thus ensuring a minimum quantity of particles for the determination of the PSD according to the international standard ISO 13322-1. Image processing and analysis was accomplished by using ImageJ, a free software developed at the National Institute of Health, and following a procedure analogous to that previously described in detail (Mazzoli & Favoni, 2012). In this connection, it is worth noting that the determination of the PSD in AC-supported MO hybrid catalysts from SEM micrographs was a very difficult task for several reasons. First, the detection and analysis of small MO aggregates supported on AC is quite complicated, especially when the particle size approaches that of phase contrast arising from the support (Heinemann & Soria, 1986). Second, this drawback is exacerbated by the fact that the MO particles may be present at different heights, embedded in the carbon substrate or overlapped by other particles, and because the AC is rough. Therefore, in order to overcome these shortcomings and enhance the visibility of the supported MO particles as much as possible, the

Table 3. Textural parameters for AC samples and prepared AC-MO hybrid catalysts

Series	Sample	S_{BET}/m^2 g^{-1}	W_0/cm^3 g^{-1}	V_{me}/cm^3 g^{-1}	V_{ma}/cm^3 g^{-1}	$V_T{}'$/cm^3 g^{-1}
AC	AC	711	0.36	0.15	0.21	0.72
samples	AC200	745	0.37	0.14	0.18	0.69
	AC850	746	0.37	0.14	0.20	0.71
Series 1	A200	556	0.27	0.13	0.16	0.56
	F200	618	0.29	0.13	0.14	0.56
	Z200	651	0.31	0.18	0.20	0.69
	S200	302	0.15	0.08	0.13	0.36
	T200	776	0.35	0.13	0.19	0.67
	W200	646	0.32	0.15	0.17	0.64
Series 2	A850	759	0.34	0.14	0.19	0.67
	F850	694	0.31	0.17	0.18	0.66
	Z850	834	0.32	0.15	0.18	0.65
	S850	680	0.33	0.16	0.18	0.67
	T850	847	0.37	0.14	0.20	0.71
	W850	741	0.35	0.15	0.20	0.71

intensity of the background was determined and subtracted from the original SEM micrographs. For such an aim, a Gaussian blur filter with a high value for the radius (here, typically 25 pixels) was applied to the original micrograph, thus generating an image of the background. The filtered image was then subtracted from the original one. Finally, the PSD was estimated directly from the resulting background-subtracted image after adjusting its brightness and contrast properly.

On the other hand, it should be noted that for spherical particles, size is defined by a single number (i.e. the diameter). Nevertheless, real situations are considerably more complicated owing to particles usually have very irregular shapes, so that assuming them as regular geometrical shapes leads to an oversimplified approximation. A variety of parameters have been proposed to define the size of irregular particles. Among them, the Feret's diameter (d_F) is one of the most commonly used, and it can be determined by ImageJ software. This diameter is defined as the longest distance between two parallel tangents on opposite sides of the image of the particle (Mazzoli & Favoni, 2012). In this work, d_F has been considered to be the best parameter for defining both the shape and size of the MO particles supported on AC surface. Table 4 summarizes the number of micrographs, the total number of particles counted and the average d_F value for each hybrid catalyst.

Results and discussion

AC and AC samples

First, it is worth noting that the morphological features of ACs are strongly dependent on the feedstock and the experimental method followed in its preparation. Because of the lack of information concerning the precursor material and the manufacture process for the commercial AC used in this work, it

Table 4. Number of micrographs, total number of particles counted and average particle size corresponding to the particle size analyses for each hybrid catalyst

Series	Hybrid catalyst	Number of images (N)	Total number of particles counted	Average particle size (d_F) nm^{-1}
Series 1	A200	4	16416	299.0
	F200	4	11880	42.7
	Z200	4	10170	757.1
	S200	4	17351	240.8
	T200	6	7596	212.9
	W200	6	1600	562.2
Series 2	A850	4	10928	393.9
	F850	7	69747	400.6
	Z850	–	–	–
	S850	7	4188	3758.5
	T850	4	6975	655.9
	W850	5	20688	1796.6

is evident that meaningful conclusions about the origin of its morphology cannot be confidently drawn. Figure 1 shows selected SEM micrographs for the raw AC. As can be seen, the particles of this carbon material exhibit a very irregular and wrinkled external surface, plenty of cracks, crevices, fissures and slits, together with smooth open pores of variable sizes. These crevices are considered to be shrinkage cracks produced during the carbonization of the precursor material (Marsh & Rodríguez-Reinoso, 2006) or developed as a result of thermal stress on the carbon matrix due to temperature changes in the activation process (Achaw & Afrane, 2008). A large number of macropores with different widths are observed in Figure 1(B), thus suggesting AC possesses a well-developed and heterogeneous macroporosity. These results are in line with the relatively high macropore volume estimated for this
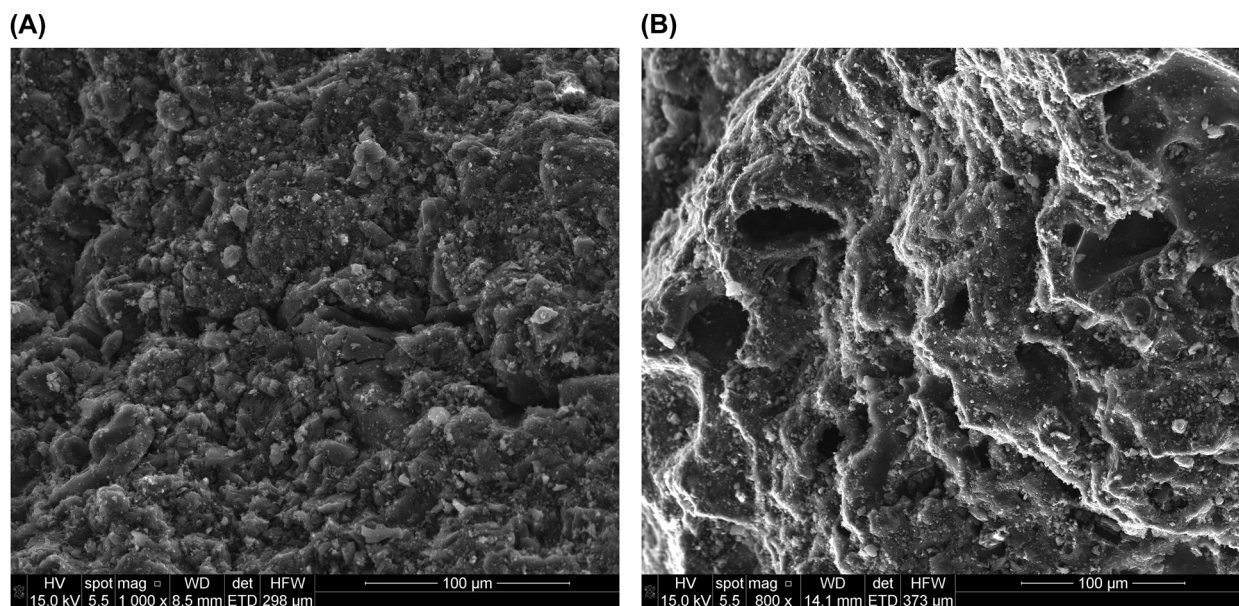
(A)

(B)

Fig. 1. Selected SEM micrographs for the raw AC.

carbon sample (i.e. $V_{ma} = 0.21$ cm^3 g^{-1}) and with its mercury intrusion curve previously reported elsewhere (Barroso-Bogeat *et al.*, 2014). Furthermore, macropores have a variety of shapes (ellipsoidal, elongated, round and so on) and their distribution over the AC surface appears to be homogeneous and entirely random in nature. These large pores on the surface are connected with a whole network of smaller pores in the inner carbon.

On the other hand, the appearance of some white dots irregularly dispersed over the carbon surface is likely connected with the ash content of AC, which has been estimated to be 4.72 wt.%. Such ash content comes from the mineral matter present in the precursor (Matos *et al.*, 2011), which remains in the carbon matrix after the preparation process of AC. As evidenced by powder XRD, ashes are mainly composed of mullite and SiO$_2$ (Barroso-Bogeat *et al.*, 2014). These results are in accordance with those obtained from EDX analysis, which indicates a relatively high silicon content (i.e. $\sim$2.76 wt.%) in AC surface, together with traces of other minority elements such as sulphur, aluminium, iron and potassium.

SEM observations were also performed on samples AC200 and AC850 in order to elucidate the morphological changes, if any, occurring in the raw AC as a result of its heat treatment under the same conditions as in the preparation of the two series of hybrid catalysts. It becomes apparent that the heat treatment of AC at 200ºC or 850ºC in inert atmosphere does not cause significant changes in its morphology, so that the micrographs obtained for AC200 and AC850 have been omitted for the sake of brevity. Therefore, the morphological changes observed for the hybrid catalysts will be mainly

due to the chemical and heat treatments carried out in their preparation.

Series 1. An irregular distribution of brighter particles over the darker external surface of AC is observed from the SEM micrographs for the hybrid catalyst A200 in Figure 2. According to XRD measurements, such particles are identified as alumina (Al$_2$O$_3$) with a very poor degree of crystallinity, as evidenced by its little mean crystallite size (i.e. $\sim$1.9 nm). As previously discussed elsewhere (Barroso-Bogeat *et al.*, 2015), alumina is likely formed by dehydration during the heat treatment at 200ºC of the bayerite (α-Al(OH)$_3$) deposited onto the AC surface after its impregnation with Al(NO$_3$)$_3$ aqueous solution and subsequent oven-drying at 120ºC. The transformation of bayerite into η-alumina usually occurs at around 230ºC, a temperature somewhat higher than that employed in the preparation of A200. The lower transition temperature for bayerite in this work may be attributable to its small crystallite size, since it has been shown that the size reducing of bayerite decreases the onset temperature of its transformation into alumina (Du *et al.*, 2009). Alumina particles on the outer surface of AC are very irregularly shaped and show a wide size distribution, with predominance of those particles having dimensions in the nanoscale. This latter assertion is also corroborated from the PSD histogram in Figure 2(B). From this figure, it follows that this hybrid catalyst has a relatively broad PSD up to ca. 2 μm, with particles mainly below 0.4 μm in size and an average diameter of 299.0 nm. Furthermore, as seen in Figure 2(A), alumina is found on AC surface not only as single particles but also forming aggregates of variable dimensions, especially at the entrance of the wider open pores. On the other
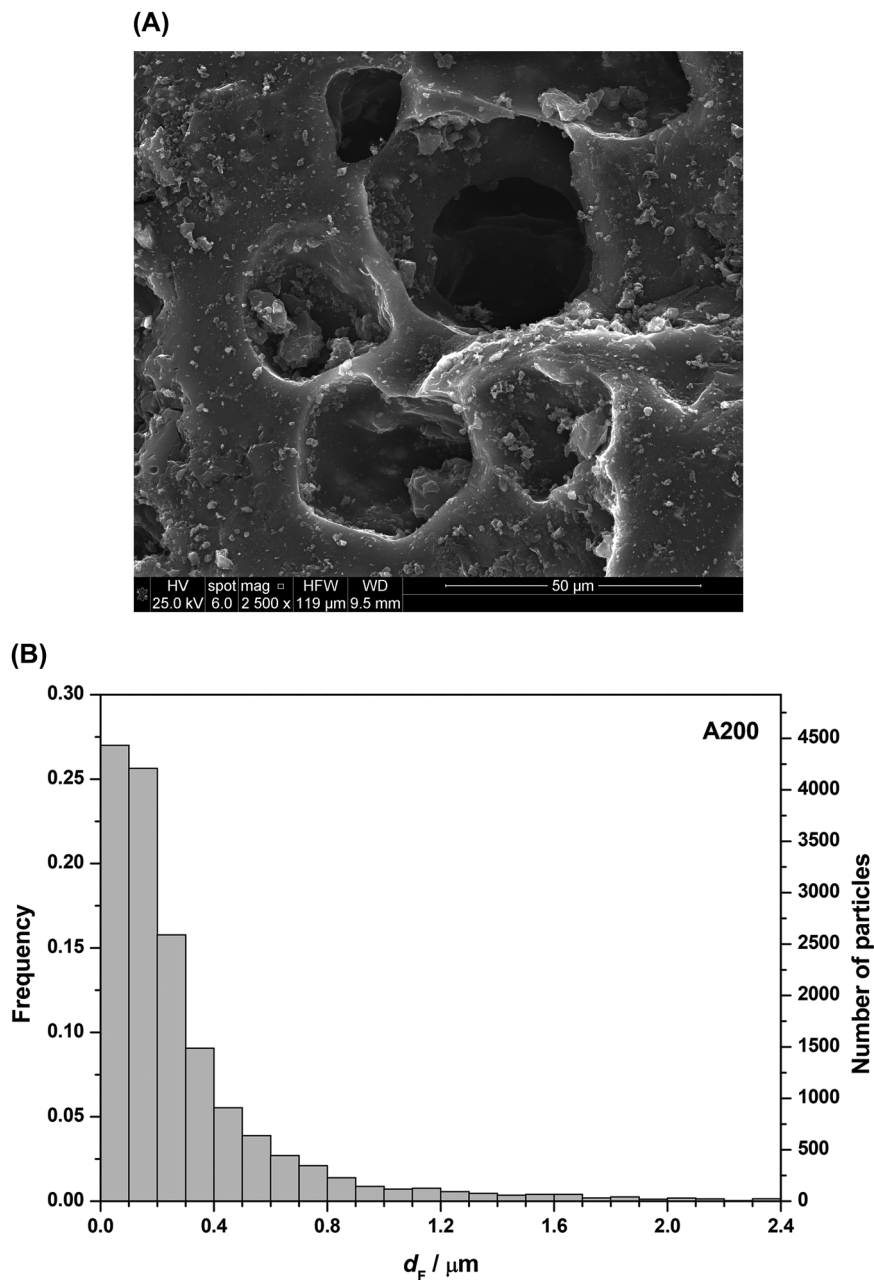
(A)

(B)

Fig. 2. Selected SEM micrographs for A200 (A), PSDs for A200 (B) and A850 (C).

hand, S_{BET} and pore volumes (Table 3) are markedly lower for A200 as compared to the raw AC, thus indicating that a large number of alumina particles have grown inside the pores of the carbon substrate.

The representative SEM micrograph of the hybrid catalyst F200 in Figure 3(A) reveals the formation of a large number of small iron-containing particles, which appear to be homogeneously dispersed over the AC surface. Powder XRD results indicate that these particles mainly consist of goethite (α-FeO(OH)) and hematite (α-Fe$_2$O$_3$) in almost equal proportions,

together with low amounts of magnetite (Fe$_3$O$_4$). Hematite is directly formed from the goethite supported on AC as a result of the impregnation and oven-drying steps, through a dehydration reaction promoted by the heat treatment at 200°C (Barroso-Bogeat *et al.*, 2015). This conversion is supposed to be a topotactic transformation occurring without the formation of any intermediate phase (Watari *et al.*, 1983); however, some author (Lima-de-Faria, 1967) reported the formation of magnetite during the goethite to hematite conversion carried out in vacuum or inert atmosphere, which may
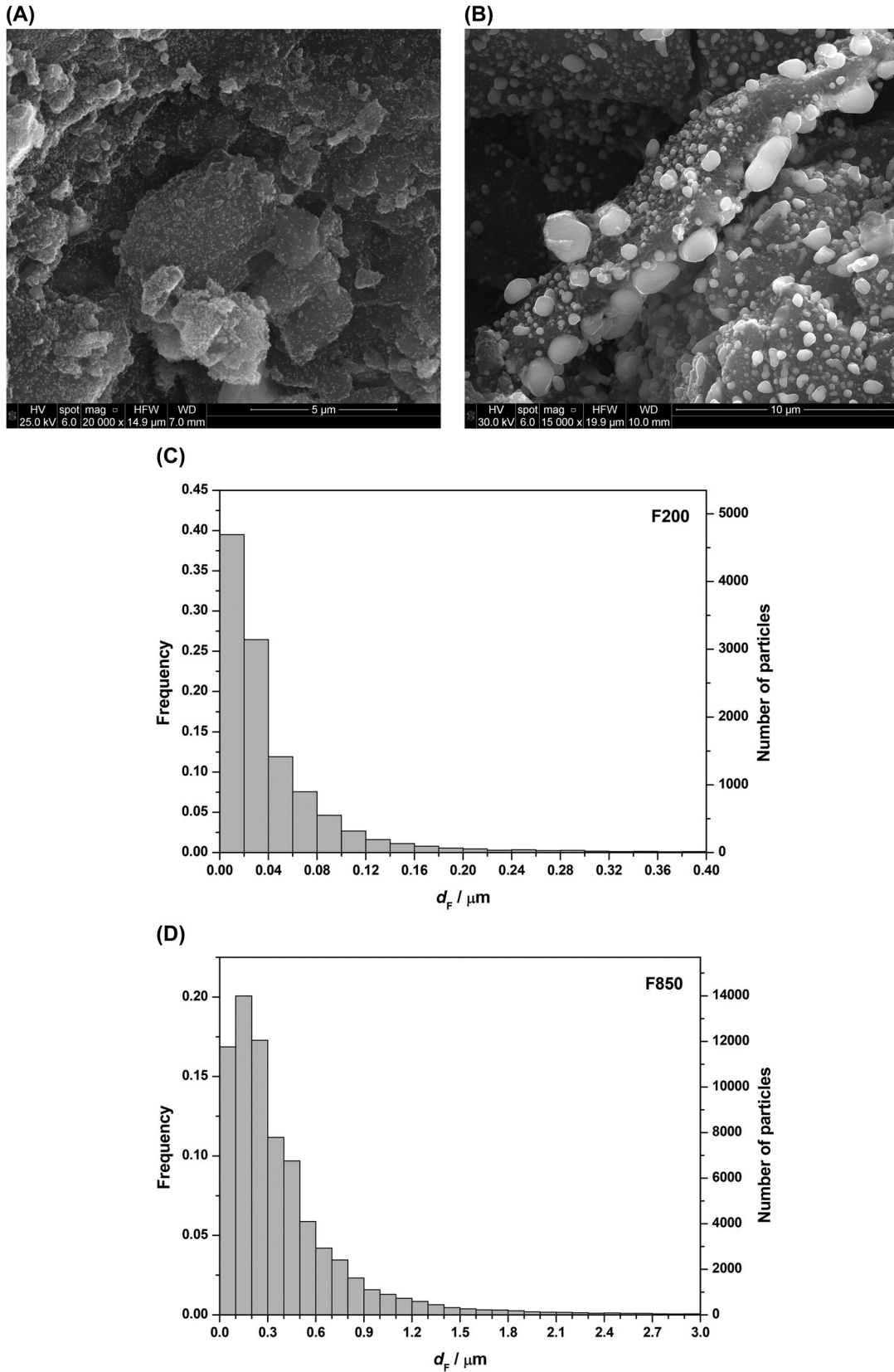
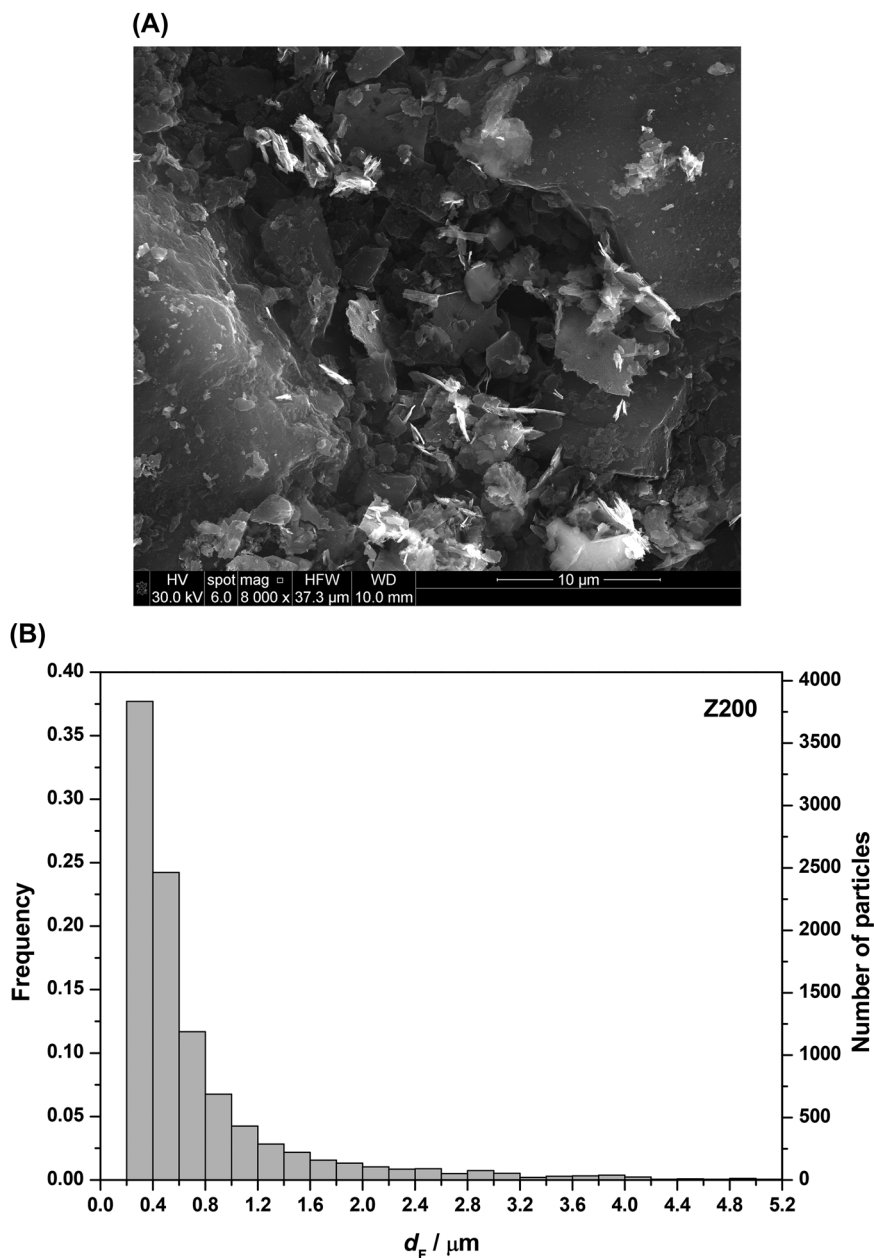Fig. 3. Selected SEM micrographs and PSDs for F200 (A and C) and F850 (B and D).

(A)

(B)

Fig. 4. Selected SEM micrographs and PSD for Z200.

explain the small amounts of magnetite detected in F200. The nanometric dimensions of the iron-containing particles supported on AC surface are confirmed from its PSD, which is illustrated in Figure 3(C). From this histogram, it follows that particles show a narrow size distribution, with more than 90% of them below 100 nm in size and an average d_F of 42.7 nm. The mean crystallite sizes estimated for goethite, hematite and magnetite from XRD measurements were 3.2, 3.2 and 6.2 nm, respectively, much smaller than the average particle size obtained from the PSD. Therefore, it becomes

apparent that the supported iron oxide nanoparticles mainly consist of aggregates of tiny crystallites.

Comparison of SEM micrographs for the raw AC (Fig. 1) and the hybrid catalyst Z200 (Fig. 4A) reveals a heterogeneous coverage of brighter particles over the external surface of the carbon substrate. The XRD pattern for sample Z200 (not shown) exhibit peaks assigned to the hexagonal ZnO with the structure of zincite and also to wülfingite (ε-Zn(OH)$_2$), the former being directly obtained from the latter by a partial dehydration during the heat treatment at 200°C. In this connection,
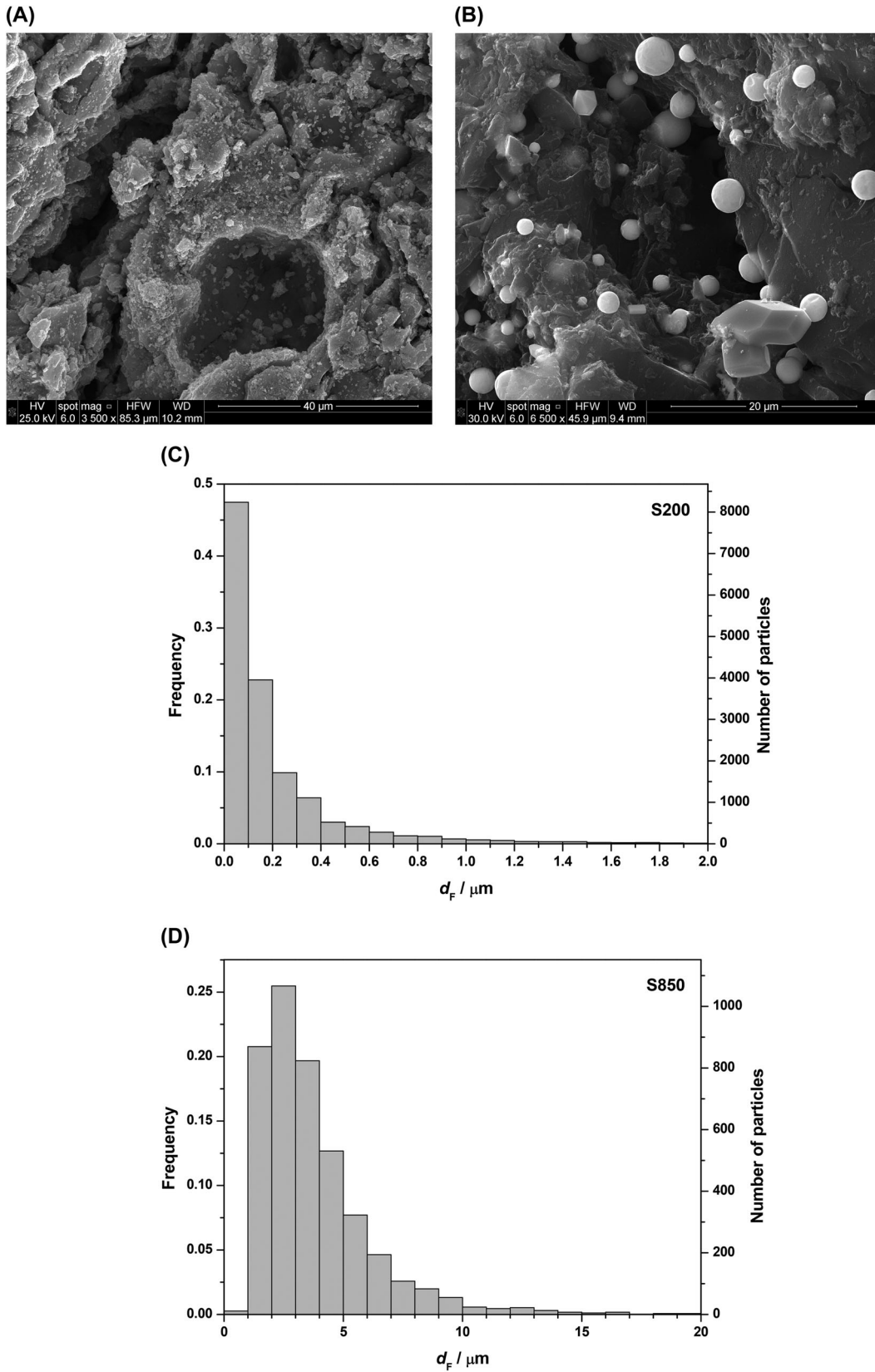
Fig. 5. Selected SEM micrographs and PSDs for S200 (A and C) and S850 (B and D).

it has been reported that wülfingite loses water at an appreciable rate at 120ºC (Leith, 1977), lower than that applied in the preparation of Z200, which explains the formation of zincite. Unlike the irregular shape observed for the MO particles in catalysts A200 and F200, Figure 4(A) shows that supported particles on the surface of Z200 display two very different morphologies. First, one observes thin sheets with variable dimensions in the microscale and relatively poor contrast as compared to the carbon support. Such morphology is typical of layered wülfingite, thus confirming its incomplete dehydration upon heating at 200ºC. The surface of these sheets is as a rule quite smooth, although some of them contain cracks likely due to the thermal decomposition, whereas the edges are serrate. Second, smaller and brighter particles identified as zincite grow not only on the aforesaid wülfingite thin sheets but also on the external surface of AC. These particles exhibit a striking morphology as they appear to form aggregates of very fine sheets and needles of variable sizes and intersecting at variable angles, according to that reported elsewhere (Pulido Melián *et al.*, 2009). From crystallite size measurements, one infers that such sheets consist of an assembly of zincite nanocrystals with an average diameter of 20.8 nm. The PSD plotted in Figure 4(B) shows a wide distribution of sizes ranging from 0.2 to 6 μm with a mean d_F of 757.1 nm, much larger than those estimated for catalysts A200 and F200, which are also prepared from the corresponding metal nitrates in aqueous solution.

Selected SEM micrograph for the hybrid catalyst S200 is shown in Figure 5(A). From this image, it is seen that brighter particles appear evenly dispersed on the darker external surface of AC after the heat treatment at 200ºC, resulting in a rougher surface for S200. The powder XRD pattern for this sample (not shown) reveals that the supported particles are composed of two different tin oxides, mainly cassiterite (SnO_2) and low amounts of romarchite (SnO). The latter is formed during the heating at 200ºC by means of a partial reduction of the cassiterite supported on AC after its impregnation with $SnCl_2$ aqueous solution and subsequent oven-drying at 120ºC. Tin oxide particles are irregularly shaped and exhibit variable sizes from nanoscale to microscale, with predominance of those having small sizes (i.e. nanoparticles) although some large clumps are also found. This observation is corroborated from the PSD for S200 in Figure 5(C), which indicates a broad distribution of sizes with around 70% of the particles having a diameter below 200 nm. The mean particle size is estimated to be 240.8 nm. Similar to other samples, the very small average crystallite size calculated both for SnO_2 and SnO by XRD (i.e. 4.1 and 5.1 nm, respectively) suggests that the brighter particles in the S200 micrograph are aggregates of these small crystallites. Furthermore, from textural data in Table 3, it is evident that the supported tin oxide particles cause a significant decrease in the three porosity regions for S200 as compared to AC, being stronger by microporosity > mesoporosity > macroporosity.

Morphological studies for the hybrid catalyst T200 are depicted in Figure 6. Upon impregnation with TiO_2-anatase powder aqueous suspension and heat treatment at 200ºC in inert atmosphere, it is seen that anatase is not uniformly distributed over the external surface of AC. By contrast, it appears to concentrate on certain regions of the carbon surface forming a relatively integrated layer with nearly uniform thickness, whereas vast surface areas of the support remain uncovered by TiO_2. Detailed examination reveals that such layer consists of aggregates of nanosize fine particles with roughly spherical shape and little aggregation degree, resulting in a puckered and spongy texture rather similar to that previously reported elsewhere (Ao *et al.*, 2008; Wang *et al.*, 2009). The PSD histogram for T200 is given in Figure 6(C). From this figure, it is evident that the TiO_2 particles forming the aggregates show a relatively broad distribution of sizes up to 1.0 μm with the main particle sizes being below 0.3 μm, thus confirming their essentially nanometric dimensions. In addition to the aforesaid larger aggregates, rather small clusters of TiO_2 particles are also found to be widely spread onto the surface of the carbon substrate (Fig. 6A). The trend of TiO_2 particles to concentrate on the external surface of AC is explained on the basis of the large particle size (i.e. lower than 44 μm) of the anatase powder employed as precursor in the preparation of T200. Anatase is not soluble in water, so that colloidal particles remain in suspension in the aqueous medium as a result of the electrostatic interaction with the dipoles of water molecules. Moreover, the particle size of anatase in aqueous suspension may even increase due to the formation of large aggregates, provided that the surface charges of the particles are not entirely neutralized at the pH value of the suspension. Therefore, it becomes clear that the access of TiO_2 to the AC porosity during the impregnation treatment is hindered because of its colloidal particle size, which prevents it from entering a large fraction of pores, especially micropores. As a consequence, TiO_2-anatase aggregates tend to accumulate mainly on the external surface of the carbon support and, to a much lesser extent, on the walls of larger-size pores. Such an accumulation of TiO_2 on pore walls brings about a narrowing of the wider pores, thus resulting in a slight decrease of meso- and macroporosity for T200 as compared to AC, whereas microporosity remains unaltered (see data in Table 3). Furthermore, supported anatase particles did not undergo any structural modification or chemical reaction during the heat treatment at 200ºC in inert atmosphere, since this TiO_2 polymorph is the only crystalline phase detected in T200 by XRD.

A representative SEM micrograph for the hybrid catalyst W200 is depicted in Figure 7(A). One notes that W200 displays a surface morphology rather similar to that for the raw carbon support, being only noticeable the presence of few brighter particles irregularly settled on the external surface of AC. These particles were identified as tungstite ($WO_3 \cdot H_2O$) and WO_3 by powder XRD. Tungstite is directly formed on the AC surface from the WO_4^{2-} ion in aqueous solution during the
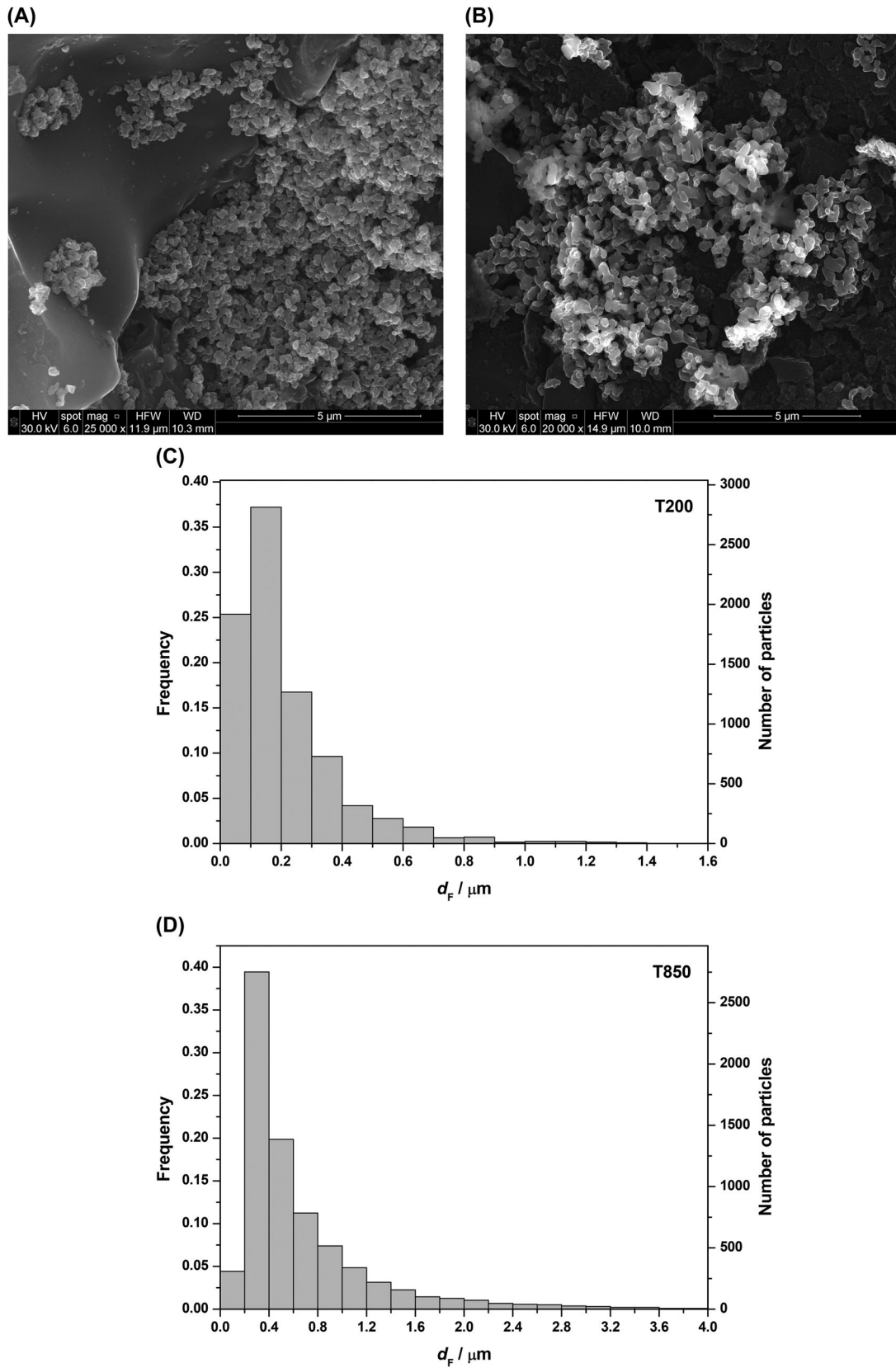
(A)

(B)

(C)

(D)

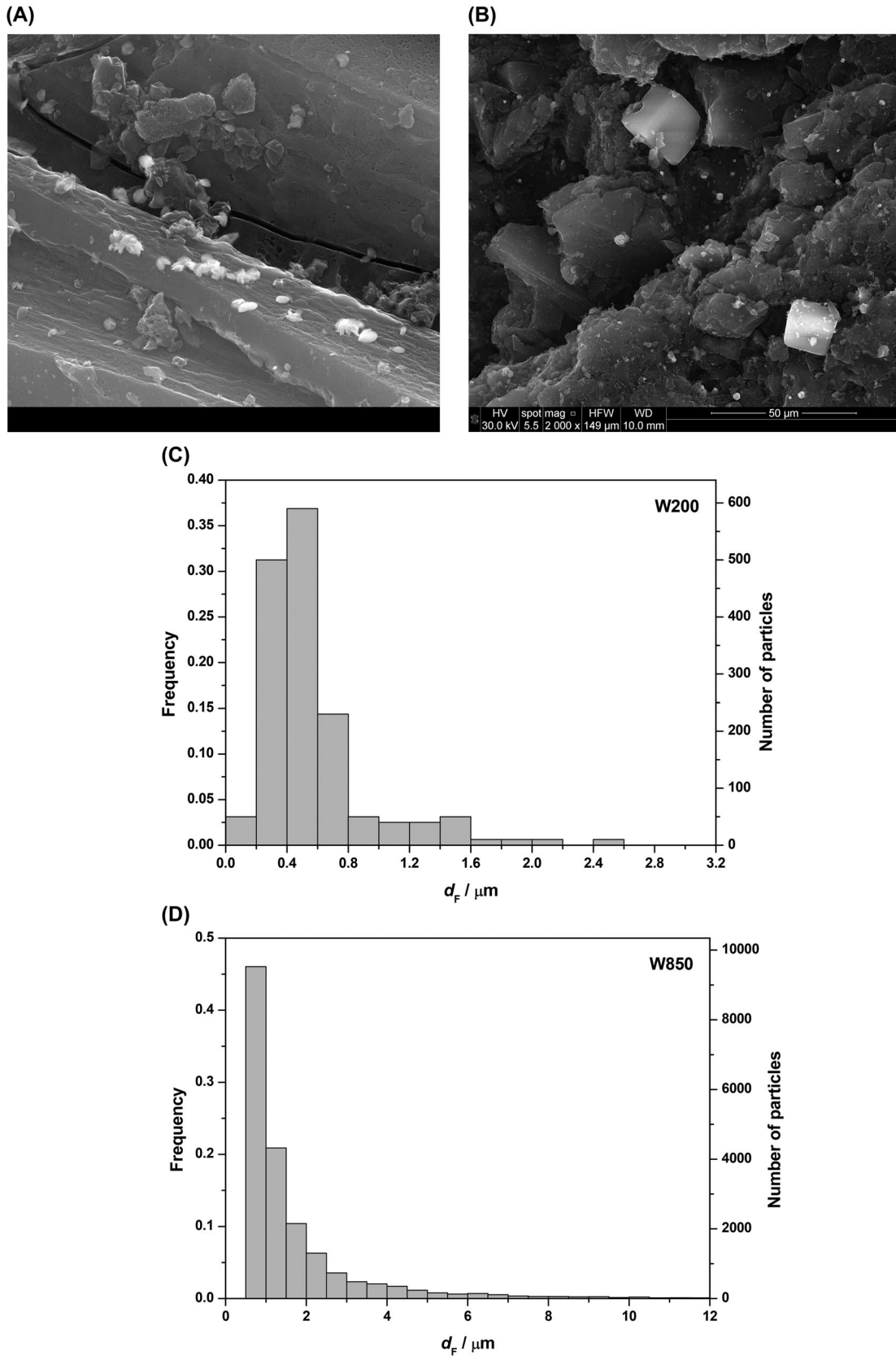**Fig. 6.** Selected SEM micrographs and PSDs for T200 (A and C) and T850 (B and D).

Fig. 7. Selected SEM micrographs and PSDs for W200 (A and C) and W850 (B and D).

impregnation process (Cotton & Wilkinson, 1986), whereas WO_3 appears as a dehydration product of the former due to the heat treatment at 200ºC (Barroso-Bogeat *et al.*, 2015). When micrographs are carefully examined, it is seen that the single particles supported on the outer surface exhibit a leaf-shaped nanoplatelet morphology, which closely resembles to that recently reported for tungstite nanoparticles synthesized from dilute $Na_2WO_4 \cdot 2H_2O$ solutions by acidification and subsequent aging at room temperature (Ahmadi & Guinel, 2014). In addition, such tungstite nanoleaves can be heat-treated at relatively low temperatures (i.e. 300ºC) to provide WO_3 nanoparticles preserving the original morphology (Ahmadi *et al.*, 2014). Moreover, tungstite and WO_3 grow on AC not only as single nanoleaves but also as aggregates with varied shape and size. From the PSD in Figure 7(C), it follows that the main particle sizes are below 2 μm, with most particles having sizes in the range from 0.2 to 0.8 μm. The mean particle size is 562.2 nm, well in agreement with the results obtained for the aforesaid tungstite nanoleaves (Ahmadi & Guinel, 2014). In spite of the large size in the micrometric scale exhibited by the particles supported on the external surface, a great number of particles are also incorporated inside the pores of the carbon substrate, as evidenced from the decrease in W_0 and V_{ma} for W200 as compared to AC (Table 3). Finally, it is worth noting that the sodium content in sample W200 coming from the Na_2WO_4 used as WO_3 precursor in its preparation was almost negligible (i.e. lower than 0.6 wt.%), as evidenced by EDX analyses.

Series 2. SEM micrographs for the hybrid catalyst A850 are quite similar to those registered for its counterpart prepared at 200ºC, so that they have been omitted for the sake of brevity. Therefore, it becomes clear that the rise of the heat treatment temperature from 200ºC to 850ºC in the preparation of the AC-alumina catalysts does not result in additional morphological changes. Likely, the most relevant modifications for A850 as compared to A200 are connected with the microstructure of the alumina phase supported on AC. Thus, whereas the alumina particles detected in A200 are essentially amorphous, those observed in A850 adopt the crystalline arrangement of α-alumina (i.e. corundum), the most stable alumina polymorph. The presence of α-alumina in A850 is striking as it only forms from bayerite at temperatures above 1200ºC (Digne *et al.*, 2002). Similar to A200, the formation of α-alumina during the preparation of A850 is likely attributable to the small particle size of the original bayerite (Du *et al.*, 2009). The PSD for A850 closely resembles that for A200 (Figs. 2B and C, respectively), being only noticeable a shift of the mean particle diameter from 299.0 nm for A200 to 393.9 nm for A850. Furthermore, an important reduction in the ash content occurs for A850 (Table 2), thus revealing a certain loss of inorganic matter during the heat treatment at 850ºC, and thereby a porosity increase in the three regions of pore sizes, as evidenced from textural data in Table 3. Such behaviour may be related to

the formation of some transient amorphous alumina with enhanced reactivity, which is reduced by the carbon substrate yielding elemental Al. This metal undergoes vaporization at temperatures above its melting point (i.e. 660.5ºC), which explains the reduction of the Al content on the catalyst surface from 6.1 wt.% for A200 to 4.6 wt.% for A850.

A representative SEM micrograph of the hybrid catalyst F850 is collected in Figure 3(B). This image reveals that the external surface of AC is covered by lots of well-dispersed particles after its impregnation with $Fe(NO_3)_3$ aqueous solution and the subsequent heat treatment at 850ºC under inert atmosphere. Detailed examination indicates that the supported particles are irregularly shaped without predominance of any defined geometric shape, and exhibit a wide range of sizes from nanoscale to microscale. Thus, the PSD obtained for F850 (Fig. 3D) shows the typical long tail to the right reported for a variety of heterogeneous catalysts when subjected to heating at high temperatures. In this case, the average particle size is 400.6 nm, much larger than for the particles in the sample F200 (i.e. 49.8 nm), suggesting the involvement of some sintering mechanism during the heat treatment at 850ºC. According to XRD results (Table 2), three different iron phases are identified for the particles in F850. They are two stable Fe_2O_3 polymorphs (i.e. hematite, α-Fe_2O_3, and maghemite, γ-Fe_2O_3) and elemental Fe. As stated above, hematite is formed by direct dehydration of goethite. However, the formation of maghemite is striking as this polymorph is only obtained directly from goethite when heating in air and in the presence of organic matter (Cornell & Schwertmann, 2003). Elemental Fe is likely formed through the carbothermic reduction of Fe_2O_3 by the carbon support. In this regard, it should be noted that the ash content is slightly higher for F850 than for F200 (Table 2), thus suggesting that no loss of iron occurs during the heat treatment at 850ºC. By comparing SEM micrographs for F850 and F200, it becomes apparent that the rise of the heat treatment temperature from 200ºC to 850ºC results not only in the aforementioned chemical reactions involving different iron compounds, but also in a migration of the iron-containing particles from the inner of the porous network to the external surface of AC and their subsequent sintering. This assertion is confirmed from EDX analyses, which reflect an increase in the surface iron content from 18.7 wt.% for F200 to 21.2 wt.% for F850. In addition, textural data show a significant increase in S_{BET} and pore volumes for F850 as compared to F200, being higher for V_{me}.

As far as catalyst Z850 is concerned, no expressive morphological modifications are verified as compared to the raw carbon substrate, so that its SEM micrographs have not been included. Indeed, ZnO particles are not clearly visible on the external surface of AC, even though XRD measurements confirm the presence of zincite crystallites with an average size of 69.4 nm. The most noticeable change for this hybrid catalyst is related to its surface composition. As seen in Table 5, the zinc content on the catalyst surface dramatically decreases

Table 5. Surface elemental composition determined by EDX analysis for AC samples and prepared AC-MO hybrid catalysts

Series	Sample	Surface elemental Carbon	Composition / Oxygen	wt.% metal
AC samples	AC	86.7	6.3	–
	AC850	88.7	6.0	–
Series 1	A200	79.0	12.4	6.14
	F200	57.8	19.0	18.70
	Z200	73.8	8.3	7.73
	S200	19.6	17.1	52.13
	T200	79.0	11.1	5.45
	W200	81.0	8.1	4.09
Series 2	A850	82.7	8.3	4.57
	F850	69.0	5.8	21.23
	Z850	85.1	8.6	0.24
	S850	60.6	4.8	29.74
	T850	78.4	10.2	5.98
	W850	83.0	6.9	7.38

from 7.7 wt.% in Z200 to 0.2 wt.% for Z850. Such a strong compositional change is believed to come from the carbothermic reduction of zincite by the AC support, yielding elemental zinc. This process is only favourable from a thermodynamic standpoint at temperatures above ~1180ºC (Barroso-Bogeat *et al.*, 2015). Nonetheless, the reduction of ZnO in the presence of a dispersive carbon phase has been suggested to occur at 650ºC (Seredych *et al.*, 2012). Because of its low melting point (i.e. 419.7ºC), elemental zinc should vaporize rapidly during the heat treatment at 850ºC in the preparation of Z850, thus resulting in a mass loss and thereby in a large porosity development for this sample as compared to Z200 (Table 3).

Figure 5(B) shows a selected SEM micrograph for the hybrid catalyst S850. It is clearly seen that the darker external surface of AC is evenly covered by a very large number of brighter particles with roughly spherical shape and quite smooth surface, although a few polyhedral particle geometries are also observed to a much lesser extent, suggesting a high degree of crystallinity. From the PSD histogram in Figure 5(D), it follows that S850 shows a very broad distribution with most particles having sizes between 1 and 10 μm; the average particle size is estimated to be around 3.8 μm and the number of particles with sizes below 1 μm is almost negligible (i.e. less than 0.3%). Unlike sample S200 and because of their relatively large size, particles in S850 are mainly located on the external surface of AC, as well as at the entrance of the wider open macropores and inside the cracks and crevices (Fig. 5B). Therefore, they are not able to effectively block the AC porosity, as evidenced from textural data in Table 3. According to XRD results, particles observed in S850 mainly consist of elemental Sn (β-Sn or white Sn) together with a residual amount of cassiterite. Elemental Sn is formed through two processes occurring at very different temperatures during the heating up to 850ºC. First,

SnO detected in sample S200 is very unstable and decomposes in the absence of air into SnO_2 and Sn at temperatures above 300ºC (Platteeuw & Meyer, 1956). Second, elemental Sn also comes from the carbothermic reduction of SnO_2 by the carbon support, which takes place above 630ºC (Padilla, 1977). Since the melting point of white Sn is 231.9ºC, it is evident that the elemental Sn formed by the above processes is in liquid state. This liquid metallic Sn tends to flow outside the porous carbon network and form large spherical particles on the external surface of AC by solidification during the cooling down from 850ºC to room temperature in inert atmosphere, thus explaining the morphological features observed for S850. Moreover, the pronounced reduction in the surface Sn content from 52.1 wt.% for S200 to 29.7 wt.% for S850 confirms that the metal undergoes a certain vaporization during the heat treatment at 850ºC. Finally, it should be noted that S850 micrographs bear some resemblance to those for F850 as far as the distribution in the carbon matrix of the supported metal particles is concerned. Nevertheless, they strongly differ in the average particle size, being much larger for S850 than for F850 (Table 4).

Sample T850 displays a surface morphology rather similar to that described above for its counterpart prepared at 200ºC. Similar to T200, detailed high optical magnification of T850 shows that the apparently uniform TiO_2 layer consists of aggregates of spheroidal TiO_2 particles (Fig. 6B). Nonetheless, the size of these particles seems to be markedly larger than that observed in T200, suggesting the involvement of a sintering process when the heat treatment temperature is increased from 200ºC to 850ºC, in good agreement with the results obtained for TiO_2-AC fibre composites prepared at different calcination temperatures (Yuan *et al.*, 2005). Such an increase in TiO_2 particle size is confirmed by the PSD for T850 depicted in Figure 6(D). By comparing this histogram to that for T200 in Figure 6(C), it is evident that the maximum of the distribution shifts towards larger particle sizes when heating at 850ºC. In fact, the mean particle size for T850 is 655.9 nm, much higher than that corresponding to T200. XRD results indicate the presence in sample T850 of rutile together with the original anatase, being both TiO_2 polymorphs almost in the same proportion. In this regard, rutile originates from anatase by means of a reconstructive phase transition, which has been reported to occur in the temperature range from 600ºC to 700ºC for fine powders of high purity (Hanaor & Sorrell, 2011) and for AC-TiO_2 hybrid catalysts (Tryba *et al.*, 2003). For pure anatase, this irreversible phase transition proceeds extremely fast above 730ºC (Czanderna *et al.*, 1958). Therefore, a complete transformation of the initial anatase into rutile would be expected in the case of T850 due to the heat treatment at 850ºC for 2 h. However, only half of the anatase has converted into rutile after such heat treatment. This behaviour is likely connected with the high surface area carbon matrix, which is able to alter the phase transition because of its high interfacial energy, thus resulting in the anticalcination effects for AC

matrix (Li *et al.*, 2007). Furthermore, anatase to rutile transition is accompanied by a significant rutile grain growth (Hanaor & Sorrell, 2011), which contributes to the overall increase in TiO_2 particle size observed for T850.

Figure 7(B) shows selected SEM micrograph for the hybrid catalyst W850. This image reveals some noticeable differences in the surface morphology of this sample as compared to the catalyst W200. At first sight, a large number of particles appearing as brighter spots with varied sizes and shapes are well dispersed over the darker and wrinkled external surface of AC. Notice the presence of very large particles with cubic shape together with other ones much smaller in size and without any apparent crystalline geometry. The wide range of sizes observed for the supported particles in catalyst W850 is confirmed by its PSD in Figure 7(D). From this bar graph, it becomes apparent that the particles show a broad size distribution up to 10 μm, with most particles between 1 and 2 μm in size and mean d_F of $\sim$1.8 μm. Powder XRD reveals that the supported particles are mainly identified as α-W grown in its typical cubic crystalline structure with an average crystallite size of $\sim$48.4 nm, together with low amounts of several tungsten carbides of variable stoichiometry, such as $W_6C_{2.54}$, with essentially amorphous morphology in view of its little crystallite size (D = 3.7 nm). Elemental W comes from the carbothermic reduction of WO_3 by AC during the heat treatment at 850ºC in the preparation of W850 (Barroso-Bogeat *et al.*, 2015). Such direct reduction occurs at temperatures above 700ºC (Swift & Koc, 2001), and has been explained on the basis of a high dispersion of WO_3 on the surface of AC (Álvarez-Merino *et al.*, 2000). The resulting metallic W may further react with the carbon support to yield tungsten carbides (Lassner & Schubert, 1999). Similar to F850, the formation of abnormally large W particles in W850 suggests that the carbothermic reduction of WO_3 is accompanied by the migration of the resulting W particles from the porous network to the outer surface of AC and their sintering. Both processes explain the increase in surface W content from 4.1 wt.% for W200 to 7.4 wt.% for W850. Furthermore, textural data for W850 in Table 3 evidence that the tungsten particles are mainly located on the external surface of the catalyst, so that they are not able to cause a significant decrease in the porosity of AC.

Conclusions

With the aim of improving the behaviour and performance of AC-MO hybrid catalysts, the changes occurring in the morphology and PSD as a result of their preparation under markedly different heat treatment temperatures (i.e. 200ºC and 850ºC) have been successfully studied by SEM and ImageJ processing program. From the obtained results, the following main conclusions may be drawn. The morphological features of the AC-MO hybrid catalysts, such as the PSD and the degree of dispersion of the supported metal particles, ultimately

depend on both the MO precursor and the heat treatment temperature. For the samples prepared at 200ºC, MO particles as a rule show a very irregular distribution over the external surface of AC, with a very low crystallinity and an average size below 0.6 μm. Moreover, most of these MO particles grow inside the pores of AC. By heating at 850ºC, the crystallinity of the supported metal particles improves, whereas the PSD broadens and the mean particle size significantly increases, being suggestive of the involvement of some sintering mechanism. These morphological changes are by far more relevant for catalysts F850, S850 and W850, which has been connected with the reduction of the corresponding MOs by the carbon substrate during the heat treatment at 850ºC. Such a reduction appears to occur in the pores of AC, and is followed by the diffusion of the resulting elemental metal particles towards the external surface and their subsequent coalescence, giving abnormally large particles. This conclusion is corroborated from EDX analyses, which also reveal a significant vaporization of Zn and, to a much lesser extent, of Sn and Al.

Acknowledgements

References

Achaw, O.-W. & Afrane, G. (2008) The evolution of the pore structure of coconut shells during the preparation of coconut shell-based activated carbons. *Microporous Mesoporous Mater.* **112**, 284–290.

Ahmadi, M. & Guinel, M.J.-F. (2014) Synthesis and characterization of tungstite ($WO_3 \cdot H_2O$) nanoleaves and nanoribbons. *Acta Mater.* **69**, 203–209.

Ahmadi, M., Younesi, R. & Guinel, M.J.-F. (2014) Synthesis of tungsten oxide nanoparticles using a hydrothermal method at ambient pressure. *J. Mater. Res.* **29**, 1424–1430.

Álvarez-Merino, M.A., Carrasco-Marín, F., Fierro, J.L.G. & Moreno-Castilla, C. (2000) Tungsten catalysts supported on activated carbon. I. Preparation and characterization after their heat treatments in inert atmosphere. *J. Catal.* **192**, 363–373.

Ao, Y., Xu, J., Shen, X., Fu, D. & Yuan, C. (2008) Magnetically separable composite photocatalyst with enhanced photocatalytic activity. *J. Hazard. Mater.* **160**, 295–300.

Barroso-Bogeat, A., Fernández-González, C., Alexandre-Franco, M. & Gómez-Serrano, V. (2011) Activated carbon as a metal oxide support: a review. *Activated Carbon: Classifications, Properties and Applications* (ed. by J.F. Kwiatkowski), pp. 297–318. Nova Science, New York.

Barroso-Bogeat, A., Alexandre-Franco, M., Fernández-González, C. & Gómez-Serrano, V. (2014) Preparation and characterization of activated carbon-metal oxide hybrid catalysts: textural characterization. *Fuel Process. Technol.* **126**, 95–103.

Barroso-Bogeat, A., Alexandre-Franco, M., Fernández-González, C. & Gómez-Serrano, V. (2015) Preparation and microstructural characterization of activated carbón-metal oxide hybrid catalysts.

New insights into reaction paths. *J. Mater. Sci. Technol.* DOI: 10.1016/j.jmst.2015.06.004

Benavidez, A.D., Kovarik, L., Genc, A., Agrawal, N., Larsson, E.M., Hansen, T.W., Karim, A.M. & Datye, A.K. (2012) Environmental transmission electron microscopy study of the origins of anomalous particle size distributions in supported metal catalysts. *ACS Catal.* **2**, 2349–2356.

Brunauer, S., Emmet, P.H. & Teller, E. (1938) Adsorption of gases in multimolecular layers. *J. Am. Chem. Soc.* **60**, 309–319.

Cornell, R.M. & Schwertmann, U. (2003) *The Iron Oxides. Structures, Properties, Reactions, Occurrences and Uses*. Wiley VCH, Weinheim.

Cotton, F.A. & Wilkinson, G. (1986) *Química Inorgánica Avanzada*. Limusa, México.

Cullity, B.D. (1959) *Elements of X-Ray Diffraction*. Addison-Wesley, Reading, MA.

Czanderna, A.W., Ramachandra Rao, C.N. & Honig, J.M. (1958) The anatase-rutile transition: part 1. – kinetics of the transformation of pure anatase. *Trans. Faraday Soc.* **54**, 1069–1073.

Datye, A.K., Xu, Q., Kharas, K.C. & McCarty, J.M. (2006) Particle size distributions in heterogeneous catalysts: what do they tell us about the sintering mechanism? *Catal. Today* **111**, 59–67.

Digne, M., Sautet, P., Raybaud, P., Toulhoat, H. & Artacho, E. (2002) Structure and stability of aluminum hydroxides: a theoretical study. *J. Phys. Chem. B* **106**, 5155–5162.

Du, X., Su, X., Wang, Y. & Li, J. (2009) Thermal decomposition of grinding activated bayerite. *Mater. Res. Bull.* **44**, 660–665.

Dubinin, M.M. (1975) *Progress in Surface Membrane Science* (ed. by J.F. Danielli, M.D. Rosenberg & D.A. Cadenhead,), vol. **9**, pp. 1–70. Academic Press, New York.

Hanaor, D.A.H. & Sorrell, C.C. (2011) Review of the anatase to rutile phase transformation. *J. Mater. Sci.* **46**, 855–874.

Heinemann, K. & Soria, F. (1986) On the detection and size classification of nanometer-size metal particles on amorphous substrates, *Ultramicroscopy* **20**, 1–14.

Henrich, V.E. & Cox, P.A. (1994) *The Surface Science of Metal Oxides*. Cambridge University Press, Cambridge, UK.

Lassner, E. & Schubert, W.D. (1999) *Tungsten. Properties, Chemistry, Technology of the Element, Alloys, and Chemical Compounds*. Kluwer Academic, New York.

Leith, R.M.A. (1977) *Preparation and Crystal Growth of Materials with Layered Structures*. Kluwer Academic, Dordrecht, Netherlands.

Li, Y., Zhang, S., Yu, Q. & Yin, W. (2007) The effects of activated carbon supports on the structure and properties of TiO_2 nanoparticles prepared by a sol-gel method. *Appl. Surf. Sci.* **253**, 9254–9258.

Marsh, H. & Rodríguez-Reinoso, F. (2006) *Active Carbon*. Elsevier, Amsterdam.

Matos, J., Nahas, C., Rojas, L. & Rosales, M. (2011) Synthesis and characterization of activated carbon from sawdust of Algarroba wood. 1. Physical activation and pyrolysis. *J. Hazard. Mater.* **196**, 360–369.

Mazzoli, A. & Favoni, O. (2012) Particle size, size distribution and morphological evaluation of airborne dust particles of diverse woods by scanning electron microscopy and image processing program. *Powder Technol.* **225**, 65–71.

Padilla, R. (1977) *The reduction of cassiterite with carbon*. PhD Thesis, University of Utah, Salt Lake City.

Platteeuw, J.C. & Meyer, G. (1956) The system tin + oxygen. *Trans. Faraday Soc.* **52**, 1066–1073.

Pulido Melián, E., González Díaz, O., Doña Rodríguez, J.M., Colón, G., Araña, J., Herrera Melián, J., Navío, J.A. & Pérez Peña, J. (2009) ZnO activation by using activated carbon as a support: characterisation and photoreactivity. *Appl. Catal. A* **364**, 174–181.

Rodríguez-Reinoso, F. (1998) The role of carbon materials in heterogeneous catalysis. *Carbon* **36**, 159–175.

Seredych, M., Mabayoje, O., Koleśnik, M.M., Krstić, V. & Bandosz, T.J. (2012) Zinc (hydr)oxide/graphite based-phase composites: effects of the carbonaceous phase on surface properties and enhancement in electrical conductivity. *J. Mater. Chem.* **22**, 7970–7978.

Serp, P. & Figueiredo, J.L. (2009) *Carbon Materials for Catalysis*. John Wiley & Sons, Hoboken, NJ.

Singh, A.K. (2005) *Advanced X-Ray Techniques in Research and Industry*. IOS Press, Amsterdam.

Swift, G.A. & Koc, R. (2001) Tungsten powder from carbon coated WO_3 precursors. *J. Mater. Sci.* **36**, 803–806.

Tryba, B., Morawski, A.W. & Inagaki, M. (2003) Application of TiO_2-mounted activated carbon to the removal of phenol from water. *Appl. Catal. B* **41**, 427–433.

Wang, X., Liu, Y., Hu, Z., Chen, Y., Liu, W. & Zhao, G. (2009) Degradation of methyl orange by composite photocatalysts nano-TiO_2 immobilized on activated carbons of different porosities. *J. Hazard. Mater.* **169**, 1061–1067.

Watari, F., Delavignette, P., van Landuyt V. & Amelinckx, S. (1983) Electron microscopic study of dehydration transformations. Part III: high resolution observation of the reaction process $FeO(OH) \rightarrow Fe_2O_3$. *J. Solid State Chem.* **48**, 49–64.

Yuan, R., Zheng, J., Guan, R. & Zhao, Y. (2005) Surface characteristics and photocatalytic activity of TiO_2 loaded on activated carbon fibers. *Colloids Surf. A* **254**, 131–136.